Journal of Materials Chemistry C

Rapid, solvent-minimized and sustainable access to various types of ferroelectric-fluid molecules by harnessing mechano-chemical technology

Journal:	*Journal of Materials Chemistry C*
Manuscript ID	TC-ART-06-2023-002212.R2
Article Type:	Paper
Date Submitted by the Author:	30-Aug-2023
Complete List of Authors:	Nishikawa, Hiroya; RIKEN, Center for Emergent Matter Science Kuwayama, Motonobu; RIKEN, Center for Emergent Matter Science Nihonyanagi, Atsuko; RIKEN, Center for Emergent Matter Science Dhara, Barun; RIKEN, Center for Emergent Matter Science Araoka, Fumito; RIKEN, Center for Emergent Matter Science

ARTICLE

Rapid, solvent-minimized and sustainable access to various types of ferroelectric-fluid molecules by harnessing mechano-chemical technology

Received 00th January 20xx,
Accepted 00th January 20xx

DOI: 10.1039/x0xx00000x

Hiroya Nishikawa,*[a] Motonobu Kuwayama,[a] Atsuko Nihonyanagi,[a] Barun Dhara[a] and Fumito Araoka*[a]

Recently, ferroelectric fluid, such as ferroelectric nematic liquid crystals (N_FLCs) and ferroelectric smectic A LCs (SmA_FLCs), has been of great fundamental and practical interest owing to its excellent polarization properties (e.g., dielectric permittivity, polarization, and nonlinear optical coefficient). To deeply understand the physical underpinning of such emergent ferroelectric phases and develop state-of-the-art device applications, effective preparation of various N_F molecules is essential. Herein, to expand the N_FLC molecular library, we implemented a mechanochemical (MC) technique for the production of LCs, demonstrating its high synthetic compatibility with N_F/SmA_FLCs. Chemical building blocks with high polarity can be bonded one by one through various ball-milling MC reactions, resulting in rapid access to N_FLC molecules, a series of DIO, RM734, UUZU, and BIOTN, with high yield within 2.7–7 h for 4–8 steps. For a new DIO variant, in which a terminal alkyl chain was completely removed, for the first time, we discovered the direct phase transition from the isotropic liquid from the SmA_F phase. Furthermore, the highly bistable polarization memory (~5.2 μC cm^{-2}) in the SmA_F phases was evaluated using the positive–up–negative–down (PUND) method.

Introduction

Recently, the emergent ferroelectricity in a new class of liquid crystalline (LC) phases, i.e., ferroelectric nematic (N_F) LCs[1–6] and ferroelectric smectic A (SmA_F) LCs[7,8], has been discovered in highly polar molecules (Fig. 1a). In the N_F phase, the local nematic director is nondegenerate (hence, $n \neq -n$), whereas the polarization is longitudinally coupled to the smectic layer normal in SmA_F. Such materials exhibit a wide spectrum of unique functional properties, including switchable polarization, large dielectric permittivity (>10000), large polarization density (>4 μC cm^{-2}), high nonlinear optical (NLO) activity (up to 10 pm V^{-1}), low switching voltage, and high fluidity. Moreover, notable physical phenomena[9–12] and structures[13,14] are observed owing to the coupling between the polarization and fluidity. Since these discoveries, research into molecular design and synthesis of N_FLCs and SmA_FLCs has been launched[7, 15–22] toward a clear understanding of the underlying mechanism,[23,24] and development of state-of-the-art materials based on them.[25,26] However, typical synthetic routes of LC materials are through a multistep pathway that entirely rely on the traditional solution chemical (SC) synthesis. As such, the net reaction time (NRT), excluding the purification time, takes a few, or several days to obtain target compounds. Moreover, complex reactor setups, huge quantities of solvent, and long reaction times are often required, thereby hampering efficient research, and development efforts on ferroelectric fluidics. If all or majority of the pathway in the SC process can be replaced by more efficient methodologies, sustainable and rapid synthetic access to N_FLC/SmA_FLC molecules would be realized. From the perspective of "rapid" chemical synthesis, microwave- and flow-assisted organic synthesis are indeed useful. The microwave-assisted synthesis achieves accelerated reaction rates through dielectric heating based on the coupling between microwaves and molecular dipoles or ion molecules. Thus, many chemical reaction examples have been reported using this method.[27] However, to efficiently absorb microwaves, polar solvents and/or materials need to be used and of course this way is not suitable for reactions below room temperature. Besides, the limitation of microwave absorption depth of the solvents causes a bottleneck for scaling up the process. For the flow-assisted synthesis, recently, Mandle demonstrated an automated synthesis of N_FLCs (only RM variants) using a continuous process, i.e., flow chemistry (FC) technology,[28] which is extensively employed in the industrial setting for large-scale synthesis. Compared to batch processes, the flow mode provides valuable advantages, such as handling hazardous reaction, safe gas introduction, and scale-up.[29] In fact, Mandle safely introduced H_2 gas in a reduction reaction system and rapidly produced RM variants on a gram scale (e.g., ~5 g h^{-1}). In contrast, we focus on the mechanochemical (MC) reaction using a ball-milling/screw-extruder technology (Fig. 1b), which has been employed as a powerful tool for molecular synthesis as an alternative to SC synthesis in the broad field of chemistry,

[a] RIKEN Center for Emergent Matter Science (CEMS), 2-1 Hirosawa, Wako, Saitama 351-0198, Japan. E-mail: hiroya.nishikawa@riken.jp; fumito.araoka@riken.jp
Electronic Supplementary Information (ESI) available: [details of any supplementary information available should be included here]. See DOI: 10.1039/x0xx00000x

including organic, organometallic, and supramolecular chemistry.[30,31] Recently, MC technology has been utilized for the design of sustainable organic synthesis[32–34] and development of functional materials.[35,36] This is ascribed to the MC reaction triggered by the direct absorption of mechanical energy, and can be performed under solvent-free/solvent-minimized reaction environments and air atmosphere. In addition, its short reaction time, high efficiency, and reaction selectivity are unique advantages. Although the FC method has notable advantages, bulk solvents are required to achieve effective reaction at a low reaction concentration (i.e., large amount of solvent) and prevent precipitation in a flow tube and its clogging and fouling.[37] In this respect, from the perspective of green chemistry and sustainable development, MC synthesis is an important method because it addresses the drawbacks of the FC method.

During ball milling, the major factor contributing to the MC reaction is impact force, which has its energetics linked to the Arrhenius' equation [$k = A\exp(-E_a/RT)$], similar to the SC reactions for organic materials.[38] As the frequency factor (A) and the energy profile term [$\exp(-E_a/RT)$] can be controlled separately, the MC reaction has vast potential to unlock inaccessible reactions by a typical SC method and design MC-based organic synthesis. When the MC avenue is adapted into LC materials, a couple of chemical building blocks can be linearly bonded, yielding a rod-like LC molecule (Fig. 1c), such as a typical nematogen, 4-Cyano-4'-pentylbiphenyl (5CB). The Suzuki–Miyaura MC coupling between (4-pentylphenyl)boronic acid and 4-bromobenzonitrile produces ca. 5 g (two reaction jars) of 5CB within 5 min at a high production yield of over 95%. Thus, through a step-by-step bonding of a larger number of building blocks with high polarity, N_F/SmA_FLC molecules can be effectively developed using the MC technique (Fig. 2a). In this paper, we report a systematic quick synthesis of N_F/SmA_FLCs featuring prototypal models (RM734[1], DIO[2], and UUZU[39] variants) to a new skeleton (BIOTN) using the ball-milling MC technology (Fig. 2b).

Results and discussion

MC synthesis strategies

For the MC reaction, the key mechanical energy can be induced into the system using different mechanical modes, such as impact, grinding, shearing, and compression, which are commonly performed in various electrical machines, such as ball millers (e.g., mixer and planetary mill) and extruders. For a mixer mill, reagents, and additives with one or more solid balls are loaded in a pair of reaction jars. By shaking the horizontally mounted jars at the desired frequency, the internal reagents undergo MC reaction by absorbing energy from the mechanical impact force (Fig. 1b and c) between the balls and the inner walls of the jars. Although the variables determining the MC reaction are not well clarified in the present case, the frequency of the reactive contact between the reactants may indicate the overall kinetics. Moreover, the reaction kinetics can be improved by a small amount of liquid additive, thereby accelerating the MC reaction owing to the better miscibility and mass transfer of reactants. This technique is commonly referred to as liquid-assisted grinding (LAG).[31] The amount of liquid additive is characterized by η, which is defined as the ratio of the volume of the liquid additive to the total weight of the solid reagents (i.e., the common unit of η is μL/mg = mL/g). This parameter permits a systematic cross comparison of various grinding method such as neat grinding ($\eta = 0$), LAG ($0 < \eta \leq 1$), slurrying ($1 < \eta \leq 10$), and typical SC reaction ($10 < \eta$).[29] In the present work, our MC synthesis was conducted for solvent-free (neat: $\eta = 0$) or solvent-minimized (LAG: $0 < \eta \leq 1$) condition.

Furthermore, to avoid metal contamination, we employed jars with volumes of 15 and 30 mL and balls (diameter: 12 mm, ~6 g), both of which were made of zirconia. The jars were blown by hot air from a heat gun with a temperature controller in order for the reactions during warming (Fig. S1, ESI). Unless otherwise noted, we fixed the vibration frequency at 30 Hz which maximized the frequency factor A in the present milling system. The archetypical chemical structures of the N_FLCs with different phase transition sequences are classified into three models: **Model I** (RM734[1]), **Model II** (DIO[2]), and **Model III** (UUQU-4-N[5]), which are shown in Fig. 2b. All models are developed by a rational molecular design to promote its permanent dipole moment with the introduction of electron-withdrawing groups (–F, $–NO_2$, and –CN) and polar linkers (–COO– and $–CF_2O–$), which are arranged in parallel or at an oblique to the molecular long-axis. Empirically, the candidate N_FLC molecules should have a large dipole moment of >8.5 Debye.[2,3,5,6,24,39,40,41] Thus, such molecules can be tailored by combining molecular building blocks with high polarity. For **Model I** (RM734), oxybenzoate units are arranged sequentially in the same direction via ester linkages. The molecule has a push–pull character, employed by an electron-donating group (2,4-dimethoxybenzoate) on one end and an electron-withdrawing group (*p*-nitrobenzene) on the other. **Model II** (DIO) is formed by combining the high polar units, e.g. a 4-(1,3-dioxane-2-nyl)phenyl unit and an ester linker. For **Model III** (UUQU-n-N), two fluorinated aromatic units are linked by a polar fluoromethoxy species. Thus, these molecules are constructed by ranging functional groups, i.e., ether, ester, and (cyclic)acetal, and a rigid biphenyl core. Herein, molecular building blocks, and their covalent assembly were synthesized on target molecules by the MC organic transformation. Based on this strategy, some new N_F and SmA_F LC molecules were developed.

The key MC reactions of etherification, esterification, acetalization, and cross-coupling were used in fabricating the corresponding molecular models (Fig. S2, ESI). The alkoxy group in the head unit of the model is induced by MC etherification, in which typical reagents (alkyl halide, base, and phase transfer catalyst) reacted by the LAG method. However, MC esterification is rarely reported. Zheng *et al.* used the I_2/KH_2PO_2 protocol to achieve a yield of 45%–91% within a reaction of 20 min at room temperature using a stainless-steel jar and ball.[42] Meanwhile, Dalidovich *et al.* reported the MC amidation between aromatics using uronium-based coupling reagents, Ethyl 2-cyano-2-((dimethyliminio)(morpholino)methyloxyimino)acetate hexafluorophosphate (COMU) and zirconium

jar/ball sets.[43] Similarly, this work obtained a quick production of within 20 min with a high yield of >80%. Although this work focused on amidation, it indicates the adaptation to MC esterification because COMU is a highly active reagent for common amidation and esterification. Therefore, the MC reaction has a great potential as an esterification method. **Model I**, and its derivatives can be synthesized by MC etherification and MC esterification.

For **Model II**, a 1,3-dioxane unit as the head unit is prepared by acetalization with reactants, solvents, and acid catalysts. However, its application to the MC reaction is a big challenge because water removal is impossible in the closed MC jars, unlike the SC method, whereby residual water can be easily removed from the system using a Dean–Stark apparatus. If the reaction is however terminated quickly before the backreaction occurs, the MC-acetalization may proceed.

To date, various types of MC coupling reactions, e.g., Suzuki–Miyaura (MC-SMC),[44] Miyaura–Ishiyama (MC-MIC),[45] and Sonogashira–Hagihara (MC-SHC),[46] have been reported. Based on these works, the biphenyl cores of **Model II** and **Model III** are likely tailored by MC-SMC.

For **Model III**, the introduction of the polar linker –CF_2O– often requires lithiation at low temperatures (e.g., –78 °C) in the initial stage, which is not suitable for our MC system. Thus, we attempted the synthesis of an alternative to **Model III**, referred to as UUZU: **Model IV**, which adopted ester groups[38]. In the late stage of the synthesis, the corresponding building blocks are connected by MC esterification.

Furthermore, to further utilize the MC reaction to realize new types of polar LC molecules, we designed, and synthesized **Model V**, which consists of two aryl groups via an alkynyl fragment (tolane-type LC) and a 2,6,7-trioxabicyclo[2.2.2]octane ring with a high dipole moment[47]. In the proposed model, we are focused on the various types of polar moieties that are more likely to be combined through MC-SMC, MC-MIC, and MC-SHC reactions. The molecular libraries in the present work are shown in Fig. S3, ESI. For all designed molecules, the molecular structure optimized by Molecular Mechanics program 2/Density Functional Theory (MM2/DFT) calculations and the corresponding dipole moment is shown in Fig. S4 and Table S1 in the ESI. All models showed the large dipole moment above 9 Debye, which is the afore-mentioned condition desired to induce N_F/SmA_F phases.

Rapid MC synthesis of N_FLCs.

Model I. As the starting material, methyl 2-hydroxy-4-methoxybenzoate was converted to the corresponding final products in five steps (Fig. 3a). A series of **Model I** was rapidly obtained by the step-by-step MC reaction and one-step solution process within 1.9 h of NRT except for workup and purification, which indicates the effectivity of the system. Note that it took approximately 10 min and 20 min for extraction and flash chromatography (they include the time of evaporation), respectively. In stage 1 (Fig. 3b), an alkyl chain was introduced into the head unit of **Model I** by MC etherification, that is, phenol was treated with a base (K_2CO_3), alkyl bromide, tetrabutylammonium bromide (TBAB), and dimethylformamide (DMF) (LAG: η_{total} = 0.8 mL g^{-1}). The actual photographs before/after the MC reaction are shown in Fig. 3b. For the reaction without heating, the conversion to the corresponding ester was completed in 90 min, but the reaction activity was boosted by heating at 80 °C, indicating the shortened complete reaction time of 5 min with a high yield of ca. 95% (as shown in the kinetic plots in Fig. 3b). The subsequent hydrolysis of the ester unit was also performed by the MC method using an NaOH/H_2O/*p*-dioxane (DIOX) system (Stage 2, Fig. 3c). To introduce the second oxybenzoate unit, Compound **2** again underwent MC esterification. The conversion from ester to carboxylic acid was conducted by hydrolysis under the SC condition (η > 10). MC hydrolysis was effective (NRT of ~10 min) for the small-scale reaction (~0.5 g), whereas its reactivity was reduced (NRT of 30 min) for the large-scale reaction (>1.0 g). However, both cases demonstrated a high reaction yield of ca. 95%. In stage 3 (Fig. 3d), we selected COMU/K_2HPO_4 protocol and explored the LAG effect on reactants. For **2a** (η = 0.19 mL/g), the conversion to ester sharply increased and almost reached the completion level of 97% (**3a**) after 20 min. The reaction completion was visually confirmed by the color change in the reactants.[42] Notably, the MC reaction can adapt to the amidation and esterification between aromatics. Unlike the typical esterification with a carbodiimide coupling reagent (e.g., *N*,*N*′-dicyclohexylcarbodiimide and 1-ethyl-3-(3-dimethylaminopropyl)carbodiimide), a polar liquid, such as ethyl acetate, can be used. For methyl 2,4-dimethoxybenzoate (**2c**) under the same condition, low reactivity was observed, which was improved with a liquid additive (as shown in the kinetic plots in Fig. 3d). Although the LAG ($0 < \eta \leq 1$) system does not affect the mechanical impact, this suggests that further incorporation of a liquid additive allows a good dispersion of reactants. This reaction time and yield are in good agreement with those obtained in a previous study (20 min, yield: ~80%).[42] In the next step (stage 4, Fig. 3e), we transformed aldehyde to carboxylic acid via oxidation. Here, we selected a shock-resistant oxidant, potassium peroxymonosulfate (Oxone®), and referred to the Oxone®/DMF protocol for SC oxidation.[48] Aldehyde (**3**) was treated with Oxone® (2 eq.) and DMF (η = 1) without heating for 1 h, resulting in the target carboxylic acid (**4**) with a yield of 80%. We noticed that the reactor warmed up by its self-reaction heat (~40 °C), as monitored by thermographic observation. Thus, MC oxidation was performed step-by-step (30 min × 2), resulting in a high yield of 95%. Moreover, the small amount of liquid additive made workup more convenient, i.e., the product was precipitated by directly transferring the crude into water. The final step was the MC esterification between **4** and *p*-nitrophenol. Similar to stage 3, the target compound was rapidly obtained within 20 min with a high yield of ~90–95%. Compared to the carbodiimide-based SC reaction, in which poor solubility of *p*-nitrophenol in dichloromethane (DCM), that is, the reaction of reactants with low concentration, caused the slow reaction, the proposed strategy is highly practical. Finally, to further explore the synthetic utility of this protocol, a gram-scale MC reaction was conducted under the same conditions (jar: 30 mL × 2). Total of

4 g (2 g per jar) of **5c** (RM734) was successfully obtained with a short NRT of 1.9 h.

Model II. For **Model II**, 1,3-dioxane and biphenyl moieties as the head and core, respectively, were prepared followed by coupling to afford the target product by the MC reaction. Although one step relied on the SC reaction, the total NRT of the three-step MC pathway was only 30 min (Fig. 4a). Stage 1 (Fig. 4b) is the MC acetalization by coupling between diol and aldehyde. The complete set-up for the MC acetalization by the SC method includes a Dean–Stark apparatus, reflux condenser, and so on (the photograph in Fig. 4b). The Dean–Stark apparatus is required to suppress the back reaction to aldehyde due to the resulting water. Thus, if the MC method plays an alternative role, more environmentally friendly acetal unit should be synthesized using a simple setup.

Firstly, the starting aldehyde was treated with propane-1,3-diol or 2-propylpropane-1,3-diol with *p*-toluenesulfonic Acid (TsOH). Interestingly, under the conditions (TsOH: 0.9 eq.), the acetalization was effectively proceed and was completed within 10 min in high yield (**7a**, **7b**: ~95%). Similarly, **23** was also quickly obtained under slightly modified conditions, in which triethyl orthoformate was used (η = 0.1 mL/g). Since the miscibility between water and isolated product was poor, it suggests that the backreaction to aldehyde is suppressed. For this protocol, in the case of a small amount of TsOH (0.025 eq.), the reactivity was reduced (conversion ratio: 65% after 30 min reaction time) (the kinetic plots (left) in Fig. 4b). Next, we used $ZrCl_4$ as a Lewis acid catalyst in place of TsOH. Although in the case of $ZrCl_4$ (0.025 eq.), the conversion ratio was 89% (after 30 min reaction), even small addition of $ZrCl_4$ (0.1 eq.) showed high and fast acetalization (the kinetic plots (middle) in Fig. 4b). Interestingly, the high additive level of the catalyst yields *trans*-rich 1,3-dioxane (TsOH: *trans*/*cis* = 4/1; $ZrCl_4$: *trans*/*cis* = 6.9/1), while the *trans*-poor product was obtained under low concentration conditions (TsOH: *trans*/*cis* = 1.5/1; $ZrCl_4$: *trans*/*cis* = 1.8/1). The stereochemical selectivity of the *trans*- and *cis*-1,3-dioxane isomer may be controlled thermodynamically and kinetically, respectively. Thus, the least amount of catalyst is inadequate in overcoming the energy barrier for the pathway of the *trans*-isomer, thereby kinetically producing the *cis*-isomer. Thus, MC acetalization is a useful method for the selective formation of the 1,3-dioxane moiety, which differs from typical SC acetalization, in which *trans*-rich 1,3-dioxane is selectively produced (the kinetic plots (right) in Fig. 4b). Notably, this new protocol has great potential in producing a series of a polar crystal with the *cis*-1,3-dioxane unit, which is a dopant stabilizing the N_F phase widely in the DIO variant molecules.[24]

The second stage is the carboxylation of the 1,3-dioxane derivatives. Although a few examples of MC carboxylation have already been reported, the applicable substrate is limited to aryl halide with a low yield. Thus, we relied on the SC protocol in this stage (Section 2.2 in ESI). Meanwhile, the counter aromatic core, i.e., mesogen core, was synthesized by MC-SMC (stage 3, Fig. 4c). We selected three types of biphenyl substituted with polar groups, i.e. –F, $–NO_2$, and –CN, as the target mesogen (**9a**–**c**). Although various MC-SMC reactions, such as those with $Pd(OAc)_2$/Buchwald ligands (SPhos),[31,43] and $Pd(OAc)_2$/NaCl,[49] have been reported, the MC synthesis of biphenyl derivatives is yet to be reported. To produce **9a**, we attempted to couple 4-bromo-3-fluorophenol and 3,4,5-trifluorophenylboronic acid using the existing protocols, that is, $Pd(OAc)_2$/SPhos and $Pd(OAc)_2$/NaCl system. For the $Pd(OAc)_2$/SPhos combination, CsF and 1,5-cyclooctadiene/H_2O were used as the base and additive, respectively. In the $Pd(OAc)_2$/NaCl system, K_2CO_3 was selected as the base. As a result, both reactions led to **9a** with a low yield of ~50% under T = 80 °C. This can be attributed to the fatal side reaction, such as polymerization, which may occur via nucleophilic aromatic substitution and/or reaction between the aryne generated by the elimination of fluorine atom. To avoid this problem, we used butylated hydroxytoluene (BHT) as the polymerization inhibitor and DIOX for the effective dispersion of the reactants and additives. Consequently, the yield was improved to 68% even under 1,1'-Bis(diphenylphosphino)-ferrocene]palladium(II) dichloride [$(Pd(dppf)Cl_2$], BHT, K_2CO_3, and DIOX (η = 0.5). Similarly, **9b** and **9c** were prepared by the optimized protocol. This protocol was further modified by adding water (3 eq.), decreasing reaction time to 10 min because of the efficient hydrolysis of a boronate and subsequent formation of an ate complex. In the final stage, the head, and mesogen units were combined by MC esterification, corresponding to the rapid and effective development of N_FLC molecules (reaction time: 20 min, yield: 80–88%). Similar to **Model I**, this protocol achieved high performance for poor soluble reactants, such as **9b**, and **9c** in DCM.

Model IV. For **Model IV**, we built a strategy, in which the head core and entire structure were synthesized following the protocol of **Model II**. However, half of the synthetic routes needed to rely on the SC reaction in stages 1 and 3, that is, the iodization and carboxylation of aromatic derivatives (Section 2.2, ESI). Despite this, the total NRT of the two-step MC pathway was almost 35 min (Fig. 5a). Before conducting the MC-SMC, the precursor was synthesized by SC iodization. I n stage 2, the biphenyl core was built by the MC-SMC protocol for biphenyl in **Model II**, resulting in a low conversion ratio of 40% (reaction time = 30 min). Thus, we optimized the MC-SMC protocol to generate aromatic cores. As shown in the kinetic plots in Fig. 5b, as the reaction temperature was increased from 80 to 110 °C, the conversion ratio as a function of temperature also increased. Furthermore, the change of the base from K_2CO_3 to Cs_2CO_3 exhibited a high conversion ratio (>95%), fast reaction completion (<15 min), and high yield (~90%). Although adding water additive boosted the reaction time (<10 min), the yield was slightly reduced to 83%, which can be ascribed to the side reaction owing to the elimination of the F atom from the aromatic ring. The following step was carboxylation (stage 3, Section 2.2 in ESI). The resulting carboxyl acid (**13a**,**b**) was treated with 2,6-difluoro-4-hydroxybenzonitrile by MC esterification to rapidly achieve the target compounds with a high yield of 86%.

Model V. Model V includes the sequential MC coupling pathways, i.e., MC-SHC, MC-MIC, and MC-SMC reactions, from stage 4 to stage 6 to generate the ethynyl aryl core with an NRT of 25 min. Although some reactions relied on the SC method (deprotection, orthoesterification, and iodation), the majority of the process (five of eight steps) was covered by the MC strategy, resulting in an NRT of 1.3 h (Fig. 6a). At stages 1–3 (Fig. 6b and Section 2.2, ESI), the starting carboxylic acid (3,5-difluorobenzoic acid) was sequentially transformed to the corresponding bicylo orthoester (BIO) derivative and aryl iodate (**17**). For the MC-SHC reaction in stage 4 (Fig. 6c), we chose the $Pd(PPh_3)_2Cl_2$/CuI/diisopropyl amine (DIPA) system as the reference to the typical SHC protocol in the conventional SC without further optimization. Instead of LAG, this is a slurrying method (η = 1.4) because the major contents were liquid (alkyne and base). Nevertheless, SHC has high reactivity to generate the corresponding ethynyl aryl unit (**18**) within 5 min with a high yield of 95%. Subsequently, unit (**19**) was synthesized by the MC-MIC protocol (Fig. 6d). In this stage, we assessed the reactivity to highly-polar aryl bromide (**19**) using the existing protocol ($Pd(OAc)_2$/$^tBu_3P{\cdot}HBF_4$ system) and our protocol ($Pd(dppf)_2Cl_2$/DIOX system). As a result, $Pd(dppf)_2Cl_2$/DIOX system under the conditions (80 °C, 20 min) achieved a higher conversion ratio and showed high yield (90%). In the stage 6 (Fig. 6e), The resulting ethynyl aryl (**18**) and aryl boronic acid pinacol ester (**19**) were treated by our MC-SMC protocol to achieve ethynyl biphenyl unit (**20**) followed by deprotection of triisopropyl silyl (TIPS) group (Section 2.2, ESI). In the final stage (Fig. 6f), aryl iodine (**17**) and deprotected ethynyl biphenyl parts (**21**) were linked by the modified MC-SHC protocol, in which the LAG method (DIOX, η = 0.3) was used. The modified MC-SHC reaction was completed at 80 °C for 20 min to obtain target compound (**22**). The synthetic protocols and material data are shown in Sections 2.1–2.3 in ESI and supplementary spectra (ESI).

Characterization of the N_F molecules

The polarized optical microscopy (POM) images and phase transition behaviors of the representative molecules in **Model I**, **II**, **IV,** and **V** are briefly summarized in Fig. 7, Figs. S5, and S6 (ESI). The phase transition point was determined by combining POM and differential scanning calorimetry (DSC). The detailed DSC data are shown in Fig. S7–S11 (ESI). For **Model I**, one of the archetypal N_F molecules, **5c** (RM734), has a phase sequence of N–N_F–K (K: Crystal) by cooling from the isotropic liquid (IL) phase (Fig. 7a). In a homeotropic polyimide (PI) cell, a typical isogyre was observed by the conoscopic observation in the N phase, indicating a homeotropic orientation which altered to the inhomogeneous/planer orientation in the N_F phase because of the surface-induced mismatch of the polar director. In the N_F phase, a polar topological defect, such as a 2π twist wall[50], was observed at the domain boundary. Thus, the observation of the unique defect is one of the indicators to assign the N_F phase.

In the heating process from the K phase, the N_F phase was not restored, indicating **5c** as a monotropic N_FLC. For the alternative molecules, **5a** (C3RM) and **5b** (C6RM) with relatively long peripheral alkyl chains, the entire temperature range shifted toward the low-temperature region which is ascribed presumably to the loose packing between molecules (Fig. 7b and Fig. S6, ESI). For **5a**, the N_F phase appeared below the N phase from 90 °C, followed by vitrification at approximately 10 °C. Similarly, **5b** has the phase sequence of N–N_F–G on cooling. The phase transition points, $T_{IL–N}$, and $T_{IL–NF}$, for **5a**, and **5b** are in good agreement with those of the corresponding compounds synthesized by the SC method.[19] During the heating of **5a** and **5b**, the N_F phase was recovered at the glass transition point and was eventually crystallized. Thus, the molecules categorized in **Model I** (**5a–c**) exhibit a monotropic N_F behavior. For **Model II**, **10a** (DIO) exhibits an intermediate mesophase between the N and N_F phases, i.e., M (the so-called N_s,[6] or SmZ_A[51]) (Fig. 7c). The N_F phase of **10a** was metastable similar to **Model I**. The molecule **10b** (C0F2F1F3) is a no-endcapped version of **10a**. Although we expected the strong on-axis dipole-dipole interaction to be induced by the short-range contact between the molecules of **10b** from the removal of the alkyl chain, the derivative did not exhibit any LC phases and is a polar crystal (Figs. S12, ESI). For **10c** (C0F2NO2F3) replacing the fluorine atom of **10b** with an NO_2 group, **10c** exhibits a direct phase transition from the IL to the N_F phase with the temperature window of ~17 K on cooling (Fig. 7d). In this type, a polar vortex structure with different chirality was observed,[52] like the chiral inorganic ferroelectric crystals. Although the N_F phase was barely induced, its thermodynamic stability was low. In sharp contrast, a further modified derivative, **10d** (C0F2NO2CN), with a large dipole moment of 14.9 D exhibited the direct IL–N_F phase transition and wide temperature range of the N_F phase over 100 K across almost room temperature (Fig. S6c, ESI). Unlike **10c** (**Model II**), **14a**/**14b** (**Model IV**) and **22a**/**22b** (**Model V**) showed IL–N_F–K phase transition with thermal hysteresis, indicating their N_F phases are intrinsically enantiotropic (Fig. 7e and 7f). According to the DFT calculation (Table S1, ESI), these molecules possess a small β (less than ~6°), which is an angle between the permanent dipole moment and long molecular axis, seemingly relevant to the emergence of enantiotropy.

To assess the polar behavior of the synthesized molecules (**Model I**, **II**, **IV,** and **V**), we investigated dielectric permittivity, polarization density, and second harmonic generation (SHG) because they are the distinct properties of the N_F phase. The data for the representative molecules (**5a**, **14a,** and **22a**) in each model are shown in Fig. 8 (Figs. S13, S15, and S19, ESI). The upper panels in Fig. 8a, d, and g are two-dimensional (2D) maps of the dielectric permittivity (ε') as a function of the frequency and temperature. The temperature scan of the ε' at a frequency of 1 kHz is shown in the bottom panels in Fig. 8a, d, and g. In the dielectric relaxation (DR) measurement, the frequency was fixed to 1 kHz to avoid a significant ionic effect at the low-frequency region. For **5a**, the ε' was increased up to 8800 in the N_F phase from the IL state, and its drastic reduction was observed below 40 °C (Fig. 8a) owing to the increment of the viscosity at low temperatures because the width of the dielectric window strongly depends on the frequency. This tendency was also observed in **5b** (Fig. S13a, ESI). Although an introduction of a long lateral alkyl chain induces the IL–N_F phase

transition, unlike **5c** (RM734), the viscosity increased proportional to the alkyl chain length, thereby reducing the dielectric performance. Similarly, for the enantiotropic N_FLCs, UUZU (**14b**), and BIOTN (**22b**) series, large dielectric permittivities of ~15000 and ~30000 were recorded in the N_F phase during cooling and heating, respectively (Fig. 8d and 8g).

The polarization–electric field (*PE*) hysteresis loops in the N_F phase regime for **5a**, **14a,** and **22a** are shown in Fig. 8b, e, and h, respectively. These loops were obtained from the polarization reversal current that occurred in the in-plane switching cell by the application of a triangular electric field (*E*-field) with various frequencies (10 Hz to 2 kHz). Calibration was made by subtracting the current of the paraelectric component. For all models, the typical parallelogram loops in the ferroelectric state were obtained under low *E*-field application of less than 1 kV cm^{-1}. Moreover, the coercive *E*-field increases with decreasing temperature owing to the rise in viscosity. Each series, **5a**, **14a,** and **22a** has a high polarization density (spontaneous polarization, P_s) of up to 6.7, 7.6, and 5.8 μC cm^{-2}, respectively. The complete data are shown in Figs. S14 and S15 (ESI).

Furthermore, we attempted to create the hysteresis loops of SHG depending on the applied *E*-field during the polarization switching. SHG is a powerful tool that enables us to indirectly access the spontaneous polarization and its directional sense via the signal intensity and the phase of the output light. In addition, such a fully optical technique can be scarcely influenced by ionic migration. The optical setup is shown in Fig. S16. In this experiment, we used nano-second laser pulses with the repetition frequency synchronized with the frequency of the applied AC triangular-wave voltage so as to measure SHG at only one certain moment during each cycle of the triangular-wave. Before the SHG hysteresis measurement, we investigated the SHG interferograms for the synthesized N_FLCs (Fig. S17). Subsequently, we tuned the optical phase to the condition that yielded the maximum amplitude difference in the SHG interferogram (red lines in Fig. S17). And then, the phase of the applied triangular-wave voltage was scanned from 0° to 360° to draw the loops. The obtained SHG loops after calibration for **5a**, **14a,** and **22a** are shown in Fig. 8c, 8f, and 8i, respectively. The details for the SHG hysteresis loop measurement and its calibration are provided in Supplementary Note 1 (ESI). The shape of the SHG loop agrees well with that of the corresponding *PE* loop, demonstrating a distinct ferroelectric response with a low *E*-field in the N_F phase. For these molecules, the coercive *E*-fields in the SHG loops tend to slightly higher than those in the *PE* loops. This implies that the SHG is more surface-sensitive than electrical measurements, and a higher voltage may be required for the surface polarization reversal because of the strong polar coupling between the surface and the polar molecules.

Characterization of the SmA_F molecules.

As shown in Fig. 1a, Kikuchi et al. replaced two fluorine atoms from DIO (**10a**, N_FLC) with two hydrogen ones, realizing for the first time the SmA_F phase in a single molecule (referred to as **Compound 6**[7]). Similarly, in our model (nonalkyl chain type of DIO), the N_F and SmA_F phases may be selectively tuned by exchanging the H/F atoms. Although no N_F phase emerged in **10b**, **10b** exhibits a pristine crystal with the polar structure of triclinic P1 symmetry. In contrast, **10f** (C0F0F1F3) exhibits the direct phase transition from IL to the SmA_F phase. This suggests that on-axis dipole-dipole interaction is enhanced by removing the alkyl chain results in vanishing of the N phase at the high-temperature region in **Compound 6**, thereby thermodynamically stabilizing the SmA_F phase (Fig. 9a). The full MC synthetic route of **10f** is shown in Fig. S20 (ESI). The DSC curves and corresponding POM texture of **10f** are shown in Fig. 9b and S9b (ESI). During cooling from the IL phase, the distinct exothermal peak (148 °C) corresponds to the IL–SmA_F phase transition. The corresponding enthalpy was 8.5 kJ mol^{-1}, which was approximately twice that of the IL–N_F phase transition.[5] At the IL–SmA_F phase transition point, the blocky texture grew along a smectic layer normal direction in the IL phase followed by the growth of its width. Finally, each domain was gathered, forming the SmA_F phase. Further cooling caused another phase transition from the SmA_F to the X_F phase at 11.7 °C (ΔH = 0.4 kJ mol^{-1}). In the X_F phase, the uniform birefringence in the domain was blurred.

The wide-angle X-ray diffraction (WAXD) pattern under the magnetic field (~0.5 T) shown in the SmA_F phase (130 °C) is shown in Fig. 9c (see also Fig. S21, ESI). In the 2D WAXD profile for the SmA_F phase (130 °C), we observed a sharp primal peak on the equatorial direction due to the smectic layer distance of 2.12 nm at a small-angle region and series of overtone peaks spanning the small- to wide-angle region on the equatorial direction. The halo peaks due to intermolecular interaction distance (0.36 nm) were observed in the meridional direction (normal to **n**). These WAXD profiles were analyzed in detail by performing horizontal and vertical scans within angles ϕ_1 = 60° and ϕ_2 = 80°, thereby generating one-dimensional X-ray diffraction (1D XRD) patterns (Figs. 9d, 9e, S22, and S23, ESI). The 1D XRD (ϕ_1 = 60°) curve was fitted by the Vogit function, deconvoluting five distinct peaks with the *d*-spacing following a typical lamellar correlation of d_{001}:d_{002}:d_{003}:d_{004}:d_{005} = 1:1/2:1/3:1/4:1/5, where d_{001} = 2.12 nm. The weakened and broadened overtone peaks are ascribed to the second type of disorder in the structure.[53] Compared to the original molecules (**Compound 6**[7]), the overtone peaks spanned to the wide-angle region (**B n**), indicating the presence of more strong short-range correlation, which is attributed to the non-endcapped molecular structure of **10f**. In the 1D XRD profile (ϕ_2 = 80°), a distinct peak *A* at *q* = 1.42 $Å^{-1}$ (*d* = 0.44 nm), which is shaper than that of peak *B* at *q* = 1.75 $Å^{-1}$ (*d* = 0.36 nm), was observed. Since the molecules are arranged in a lamellar layer without tilting, this phase was assigned as a smectic A phase. The layer spacing of 2.12 nm was larger than the molecular length obtained by X-ray analysis conducted for a single crystal, L_{mol} = 1.96 nm. This implies that the two molecules assemble in a dimer with an offset of ~8% along the long axis of the molecule, and two molecules may be displaced in parallel with an intermolecular distance of 0.44 nm (which was also observed in the single crystal X-ray result for **10f**, Fig. S12e and f, ESI). The

layer spacing and offset level decreased with decreasing temperature (Fig. S24, ESI).

To investigate the ferroelectric response in the SmA_F and X_F phases, DR spectroscopy and *PE* hysteresis loop measurement were performed. The DR spectra and dielectric permittivity as a function of temperature (f = 1 kHz) are shown in Fig. 10a–c, respectively. In the experiment, we used a silanized ITO cell, in which the homeotropic alignment was not observed at any temperature range. Thus, we considered an apparent relative permittivity and dielectric loss.[2,7] At the phase transition point of IL–SmA_F, a DR peak emerged around a few kHz and shifted to a lower frequency with decreasing temperature in the SmA_F phase (Fig. 10a). The dielectric permittivity reached ~7500 at 140 °C, and ε′ gradually decreased to ~1000 (Fig. 10b, c). However, the dielectric permittivity sharply increased at the SmA_F–X_F phase transition, reaching ε′ of ~6000 because of the jumping of the DR peak position from a low to a high frequency of 40 kHz (Fig. 10a). In the X_F phase, the DR peak shifted to a high frequency, which is the opposite trend to the SmA_F phase. This phenomenon and the clear characterization of the X_F phase will be further investigated and published elsewhere.

Kikuchi et al. demonstrated a memory function of the SmA_F phase using the SHG technique. For the quantitative evaluation of the remnant polarization after polarization reversal, we performed the positive–up–negative–down (PUND) polarization measurement. The PUND technique has been extensively used in ferroelectric materials because we separately evaluated the leakage current and polarization, and consequently, the true polarization values.[54–57] Firstly, a negative triangular pulse (p) was applied for pre-treatment. Subsequently, two positive (P and U), and two negative (N and D) triangular pulses were applied to measure polarization in the positive and negative polarization states, respectively (Fig. 10d). During the removal of the *E*-field for a period of retention time (t_r), the relaxation of the polarization was controlled. Thus, if the spontaneous polarization is stable during t_r, the pulse in the U (D) process does not change the polarization. In contrast, if the initial polarization was relaxed during t_r, the next U (D) pulse built up the polarization again. Thus, by subtracting such a non-ferroelectric current component of the U (D) process from the whole current component of the P (N) process, the remnant polarization can be extracted.

In our experiment, we employed the current measurement using the PUND technique to obtain "genuine" *PE* hysteresis loops. In this experiment, we measured PE hysteresis loops for two different conditions, that is, in-plane switching (IPS) and out-of-plane switching (OPS) geometries. For IPS and OPS, we used an antiparallelly rubbed homogeneous PI cell and a silanized ITO cell, respectively. The *PE* hysteresis loops without the PUND method and the temperature dependence of P_s are shown in Fig. S25 (ESI) for comparison. IPS and OPS showed similar spontaneous polarization (P_s) values of ~4.9–5.5 μC cm^{-2} over the entire range between the SmA_F and X_F phases. For the OPS, although the initial planer orientation (director did not follow the surface vertical orientation) changed to the homeotropic alignment under the *E*-field, the field removal relaxed the orientation in the SmA_F and X_F phases. The relaxation kinetics was presented by plotting $P(t_r)/P_S$, where $P(t_r)$ is the remnant polarization at t_r. In the case of OPS, the remnant polarization was dramatically reduced from ~5.0 μC cm^{-2} to ~1.1 μC cm^{-2} at t_r = 1 s (i.e., $P(1)/P_s$ = 0.2) in the SmA_F and X_F phases (gray plots in Fig. 10k and 10l). For the SmA_F phase in a thicker IPS cell (17 μm), the birefringence of the blocky texture (Fig. 10e) changed to almost dark state, meaning the uniform director orientation along the *E*-field (and the polarizer). The uniform state was maintained over 1000 s (Fig. 10f). In addition, the field-induced alignment uniformity was improved in a thinner cell (4.8 μm) (Fig. 10h and 10i). In the X_F phase, the uniform alignment was not achieved even in the thinner cell (Fig. 10g and 10j). The relaxation kinetics for the IPS in the SmA_F and X_F phases are shown in Fig. 10k and 10l (green plots) (see also Fig. S26, ESI), respectively. For both cases, only 4% reduction of the initial polarization at t_r = 1000 s ($P(1000)/P_s$ = 0.97) was observed (SmA_F: 5.4 ⟶ 5.2 μC cm^{-2}; X_F: 5.5 ⟶ 5.3 μC cm^{-2}), indicating a stronger memory effect. Such good polarization sustainability could be ascribed to the surface-stabilized effect similarly to the chiral smectic C (SmC*) ferroelectric LC, i.e., the SSFLC mode.[58]

Compatibility of MC method with discotic LC molecules.

The present paper mainly introduced the development of rod-like LC molecules using the MC method. Although there have been several reports on the MC synthesis of π-conjugated molecules[36,37] whose core designs are essentially similar to those of many discotic LC molecules, there is no specific report on the MC synthesis of discotic LC molecules, as far as we know. Therefore, it would be worth considering possible discotic LC synthesis using the MC technique. One example is based on a modification of an already-known synthesis[59] which is a solution process comprising three sequential steps: 1) etherification, 2) dibromo olefination, and 3) Sonogashira-Hagihara coupling (SHC). These synthetic pathways can potentially be replaced with MC etherification, MC-dibromo olefination, and MC-SHC techniques. Thus, the MC synthesis is expected to be utilized for many other LC systems.

Conclusions

In this study, we successfully developed a rapid approach to obtain ferroelectric fluid, particularly N_FLCs, through a powerful MC method. In this strategy, the chemical building blocks with high polarity were connected one by one via various types of MC reactions, i.e., MC etherification, MC esterification, MC acetalization, MC oxidation, and MC coupling. Although we relied on the SC synthesis for the partial reactions, such as carboxylation and iodization, an overwhelming reaction was covered by the MC synthesis, generating various types of N_FLC molecules, including from archetypal to new model. For **Model I** (RM734 variant), all reaction steps were fully covered only by the MC technique, achieving a total NRT of 1.9 h in five steps. For another model, the significantly fast reaction as MC acetalization and MC coupling (5–15 min) boosted the production of N_FLC molecules. Consequently, extremely short

NRT of **Model II** (DIO variant), **Model IV** (UUZU variant), and **Model V** (BIOTN variant) of 2.7, 7, and 5 h per four, four, and eight steps, respectively. Moreover, POM, *P*–*E* hysteresis, and SHG studies demonstrated the excellent polarization behavior of all models, i.e., large dielectric permittivity (up to 30000), high polarization (4.6–8.6 μC cm^{-2}), and high SHG activity in the N_F phase. Polarization inversion was confirmed by the SHG interference under (±) *E*-field. The change in the amplitude between two SHG interferograms induced by the (±) *E*-field led to the SHG-hysteresis loop in the N_F phase. For **Model II**, in the nonalkyl chain DIO variants, **10b** did not show the N_F phase but exhibited a polar crystal. Although **10c** displayed a narrow temperature window of the N_F phase, a wide temperature range (ΔT ~100 K) is noted for the N_F phase for **10d** even on heating. **Model III** and **Model V** were confirmed to be enantiotropic N_FLCs with direct IL–N_F phase transition. For **Model V**, the N_F phase persisted up to 300 °C within the wide temperature window of 100–150 K. For the fluorine-deficient type nonalkyl chain DIO variant, **10f**, we first observed the direct IL–SmA_F phase transition. Besides, **10f** has an additional ferroelectric fluid state (i.e., X_F phase) at the regions with lower temperature. Both phases showed ferroelectric behavior, which was revealed by DR and *P*–*E* hysteresis studies. Furthermore, we demonstrated quantitative evaluation of the remnant polarization using the PUND method in the IPS and OPS. For the IPS, a significantly high memory function was observed both in the SmA_F and X_F phases. We believe that the MC technical strategy effectively, rapidly, sustainably enriches molecular libraries of ferroelectric fluid, including N_FLC and SmA_FLC, and contributes to their fundamental and practical studies.

Author Contributions

H.N. conceived the project and performed all the experiments. F.A. co-designed the work and constructed the optical and electrical setups for SHG. M.K. co-designed a synthetic strategy and measured HRMS. A.N. synthesized compounds by SC method and reproduced MC synthesis. B.D. measured and analyzed the single crystal XRD. H.N. and F.A. analyzed data and discussed the results. H.N. and F.A wrote the manuscript and all authors approved the final manuscript.

Conflicts of interest

There are no conflicts to declare.

Acknowledgements

We are grateful to Drs. Y. Ishida (RIKEN, CEMS), H. Koshino (RIKEN, CSRS), and H. Sato (RIKEN, CEMS) for allowing us to use a NANOPIX 3.5m system (Rigaku), JNM-ECZ500 (JEOL), and QTOF compact (BRUKER), respectively. We would like to acknowledge the Hokusai GreatWave Supercomputing Facility (project no. Q22575 and Q22446) at RIKEN Advanced Center for Computing and Communication (RIKEN ACCC). We wish to thank Profs. H. Kikuchi and Y. Okumura (Kyushu University), and Mr. A. Manabe (ex. Merck KGaA) for fruitful discussions. This work was partially supported by JSPS KAKENHI (JP22K14594; H.N., JP21H01801; F.A.), RIKEN Special Postdoctoral Researchers (SPDR) fellowship (H.N.), FY2022 RIKEN Incentive Research Projects (H.N.), and JST CREST (JPMJCR17N1; F.A.) and JST SICORP EIG CONCERT-Japan (JPMJSC22C3; F.A.).

References

1 R. J. Mandle, S. J. Cowling and J. W. Goodby, *Chem. Eur. J.* 2017, **23**, 14554–14562.
2 H. Nishikawa, K. Shiroshita, H. Higuchi, Y. Okumura, Y. Haseba, S. I. Yamamoto, K. Sago and H. Kikuchi, *Adv. Mater.* 2017, **29**, 1702354.
3 A. Mertelj, L. Cmok, N. Sebastián, R. J. Mandle, R. R. Parker, A. C. Whitwood, J. W. Goodby and M. Čopič, *Phys. Rev. X* 2018, **8**, 041025.
4 X. Chen, E. Korblova, D. Dong, X. Wei, R. Shao, L. Radzihovsky, M. A. Glaser, J. E. MacLennan, D. Bedrov, D. M. Walba and N. A. Clark, *Proc. Natl Acad. Sci. U.S.A.* 2020, **117**, 14021–14031.
5 A. Manabe, M. Bermer and M. Kraska, *Liq. Cryst.* 2021, **48**, 1079–1086.
6 N. Sebastián, M. Čopič and A. Mertelj, *Phys. Rev. E* 2022, **106**, 021001.
7 H. Kikuchi, H. Matsukizono, K. Iwamatsu, S. Endo, S. Anan and Y. Okumura, *Adv. Sci.* 2022, **9**, 2202048.
8 X. Chen, V. Martinez, P. Nacke, E. Korblova, A. Manabe, M. Klasen-Memmer, G. Freychet, M. Zhernenkov, M. A. Glaser, L. Radzihovsky, J. E. Maclennan, D. M. Walba, M. Bremer, F. Giesselmann and N. A. Clark, *Proc. Natl Acad. Sci. U.S.A.*, 2022, **119**, e2210062119.
9 M. T. Máthé, Á. Buka, A. Jákli and P. Salamon, *Phys. Rev. E*, 2022, **105**, L052701.
10 P. Kumari, B. Basnet, H. Wang and Oleg D Lavrentovich, *Nat. Commun.*, 2023, **14**, 748.
11 M. T. Máthé, B. Farkas, L. Péter, Á. Buka, A. Jákli and P. Salamon, *Sci. Rep.*, 2023, **28**, 6981.
12 S. Marni, G. Nava, R. Barboza, T. G. Bellini and L. Lucchetti, *Adv. Mater.*, 2023, DOI: 10.1002/adma.202212067.
13 H. Nishikawa and F. Araoka, *Adv. Mater.*, 2021, **33**, 2101305.
14 C. Feng, R. Saha, E. Korblova, D. Walba, S. N. Sprunt and A. Jákli, *Adv. Opt. Mater.*, **9**, 202101230.
15 R. J. Mandle, *Soft Matter*, 2022, **18**, 5014–5020.
16 R. J. Mandle, S. J. Cowling and J. W. Goodby, *Liq. Cryst.*, 2021, **48**, 1780–1790.
17 D. Pociecha, R. Walker, E. Cruickshank, J. Szydlowska, P. Rybak, A. Makal, J. Matraszek, J. M. Wolska, J. M. D. Storey, C. T. Imrie and E. Gorecka, *J. Mol. Liq.*, 2022, **361**, 119532.
18 R. Saha, P. Nepal, C. Feng, Md Sakhawat Hossain, M. Fukuto, R. Li, J. T. Glesson, S. Sprunt, R. J. Twieg and A. Jákli, *Liq. Cryst.*, 2022, **49**, 1784–1796.
19 E. Cruickshank, R. Walker, J. M. D. Storey and C. T. Imrie, *RSC Adv.*, 2022, **12**, 29482–29490.
20 R. J. Mandle, *Liq. Cryst.*, 2022, **49**, 2019–2026.
21 N. Tufaha, E. Criuckshank, D. Pociecha, E. Gorecka, J. M. D. Storey and C. T. Imrie, *Chem. Eur. J.*, 2023, **29**, e202300073.
22 M. Cigl, N. Podoliak, T. Landovský, D. Repček, P. Kužel and V. Novotná., arXiv, 2023, preprint, arXiv: 2301.04865, https://arxiv.org/abs/2301.04865v1.
23 R. J. Mandle, N. Sebastián, J. Martinez-Perdiguero, A. Mertelj, *Nat. Commun.*, 2021, **12**, 4962.
24 H. Nishikawa, K. Sano, S. Kurihara, G. Watanabe, A. Nihonyanagi, B. Dhara and F. Araoka, *Commun. Mater.*, 2022, **3**, 89.
25 H. Nishikawa, K. Sano and F. Araoka, *Nat. Commun.*, 2022, **13**, 1142.
26 S. Nishimura, S. Masuyam, G. Shimizu, C.-Y. Chen, T. Ichibayashi and J. Watanabe, *Adv. Physics Res.*, 2022, **1**, 2200017.
27 M. B. Gawande, S. N. Shelke, R. Zboril and R. S. Varma, *Acc. Chem. Res.* 2014, **47**, 1338–1348.

28 R. J. Mandle, *Liq*. *Cryst*., 2023, https://doi.org/10.1080/02678292.2023.2208550.
29 M. B. Plutschack, B. Pieber, K. Gilmore and P. H. Seeberger, *Chem*. *Rev*. 2017, **117**, 11796−11893.
30 S. L James, C. J. Adams, C. Bolm, D. Braga, P. Collier, T. Friščić, F. Grepioni, K. D. M. Harris, G. Hyett, W. Jones, A. Krebs, J. Mack, L. Maini, A G. Orpen, I. P. Parkin, W. C. Shearouse, J. W. Steed and D. C. Waddell, *Chem*. *Soc*. *Rev*. 2012, **41**, 413–447.
31 J.-L. Doand and T. Friščić, *ACS Cent*. *Sci*., 2017, **3**, 13–19.
32 K. Kubota, T. Seo, K. Koide, Y. Hasegawa and H. Ito, *Nat*. *Comuun*., 2019, **10**, 111.
33 K. Kubota, Y. Pang, A. Miura and H. Ito, *Science*, 2019, **366**, 1500–1504.
34 R. Takahashi, A. Hu, P. Gao, Y. Gao, Y. Pang, T. Seo, J. Jiang, S. maeda, H. Takaya, K. Kubota and H. Ito, *Nat*. *Commun*., 2021, **12**, 6691.
35 K. Kubota, N. Toyoshima, D. Miura, J. Jiang, S. Maeda, M. Jin and H. Ito, *Angew*. *Chem*. *Int*. *Ed*., 2021, **60**, 16003–16008.
36 J. A. Leitch, H. R. Smallman and D. L. Browne, *J*. *Org*. *Chem*. 2021, **86**, 14095–14101.
37 R. R. A. Bolt, J. A. Leitch, A. C. Jones, W. I. Nicholson and D. L. Browne, *Chem*. *Soc*. *Rev*., 2022, **51**, 4243–4260.
38 J. M. Andersen and J. Mack, *Chem*. *Sci*. 2017, **8**, 5447–5453.
39 A. Manabe, M. Bremer, M. Kraska and M. Klasen-Memmer, Proceedings of the international display workshops, 2021, https://doi.org/10.36463/idw.2021.0050.
40 H. Matsukizono, K. Iwamatsu, S. Endo, Y. Okumura, S. Anan and H. Kikuchi, *J*. *Mater*. *Chem*. *C*, 2023, **11**, 6183–6190.
41 H. Kikuchi, H. Nishikawa, K. Shiroshita, S. Endo, Y. Mizuki, H. Iwaisako, S. Anan, Y. Okumura, S. Yamamoto, K. Sago and Y. Haseba, In Abstract Book of Japanese Liquid Crystal Society Online Meeting, 2020, https://doi.org/10.11538/ekitou.2020.0_2I02.
42 L. Zheng, C. Sun, W. Xu., A. V. Dushkin, N. Polyakov, W. Su and J. Yu, *RSC Adv*., 2021, **11**, 5080–5085.
43 T. Dalidovich, K. A. Mishra, T. Shalima, M. Kudrjašova, D. G. Kananovich and R. Aav, *ACS Sustainable Chem*. *Eng*., 2020, 8, 15703–15715.
44 T. Seo, N. Toyoshima, K. Kubota and H. Ito, *J*. *Am*. *Chem*. *Soc*. 2021, **143**, 6165–6175.
45 K. Kubota, E. Baba, T. Seo, T. Ishiyama and H. Ito, Beilstein *J*. *Org*. *Chem*., 2022, **18**, 855–862.
46 Y. Gao, C. Feng, T. Seo, K. Kubota and H. Ito, *Chem*. *Sci*. 2022, **13**, 430–438.
47 R. Paschke, H. Zaschke, A. Hauser and D. Demus, Liq. Cryst., 1989, 6, 397–407.
48 B.R. Travis, M. Sivakumar, G. O. Hollist and B. Borhan, *Org*. *Lett*., 2003, **5**, 1031–1034.
49 G. Báti, D. Csókás, T. Yong., S. M. Tam, R. R. S. Shi, R. D. Webster, I. Pápai, F. García and M. C. Stuparu, *Angew*. *Chem*. *Int*. *Ed*., 2020, **59**, 21620–21626.
50 Chen, E. Korblova, M. A. Glaser, J. E. Maclennan, D. M. Walba and N. A. Clark, *Proc*. *Natl*. *Acad*. *Sci*. *U*.*S*.*A*., 2021, **118**, e2104092118.
51 X. Chen, V. Martinez, E. Korblova, G. Freychet, M. Zhernenkov, M. A. Glaser, C. Wang, C. Zhu, L. Radzihovsky, J. E. Maclennan, D. M. Walba and N. A. Clark, *Proc*. *Natl Acad*. *Sci*. *U*.*S*.*A*., 2023, **120**, e2217150120.
52 K. Perera, R. Saha, P. Nepal, R. Dharmarathna, Md Sakhawat Hossain, Md Mostafa, A. Adaka, R. Waroquet, R. J. Twieg and A. Jákli, *Soft Matter*, 2023, **18**, 347–354.
53 B. K. Vainshtein, Diffraction of X-rays by Chain Molecules, Elsevier, Amsterdam, 1966.
54 M. Fukunaga and Y. Noda, J. Phys. Soc. Jpn. 2008, 77, 064706.
55 S. Horiuchi, Y. Tokunaga, G. Giovannetii, S. Picozzi, H. Itoh, R. Shimano, R. Kumai and Y. Tokura, *Nature*, 2010, **463**, 789–792.
56 S. Horiuchi, F. Kagawa, K. Hatahara, K. Kobayashi, R. Kumai and Y. Tokura, *Nat*. *Commun*., 2012, **3**, 1308.
57 A. V. Gorbunov, M. G. Iglesias, J. Guilleme, T.D. Cornelissen, W. S. Christian Roelofs, T. Torres, D . González-Rodríguez, E. W. Meijer and M. Kemerink, *Sci*. *Adv*. 2017, **3**, e1701017.
58 N. A. Clark and S. T. Lagerwall, *Appl*. *Phys*. *Lett*., 1980, **36**, 899–901.
59 J. De, A. H. M. M., R. A. K. Yadav, S. P. Gupta, I. Bala, P. Chawla, K. K. Kesavan, J. Jou and S. K. Pal, *Chem*. *Commun*., 2020, **56**, 14279–14282.

Legends of Figures

Fig. 1. a) illustration of a new concept for the development of N_F /SmA_FLCs, in which the polarization (*P*) orients unidirectionally along director (*n*), showing excellent performances. (b) Convenient tools for MC reaction, vibration ball mill, planetary ball mill, and extruder. b) illustration of a concept for the development of functional materials using the MC method.

Fig. 2. a) The MC-based synthetic strategies for building **Models I–V**. b) Key MC reaction bank. c) Target NFLC models, **Model I**: RM series, **Model II**: DIO series, **Model III**: UUQU series, **Model IV**: UUZU series, **Model V**: BIOTN series.

Fig. 3. The MC-synthesis pathway for **Model I** (RM families). Abbrev.: VM: vibration ball milling, w/o-h: without heating. Work-up and/or purification was conducted by column chromatography (CC), extraction (EX), and/or recrystallization (RC). The inserted reaction time (upper right) does not include workup time (i.e., NRT). In reality, it took approximately 10-20 minutes per one work-up process.

Fig. 4. The MC-synthesis pathway for **Model II** (DIO families). Abbrev.: VM: vibration ball milling, w-h: with heating, w/o-h: without heating. Work-up and/or purification was conducted by column chromatography (CC), extraction (EX), and/or recrystallization (RC). Note: for the gram-scale synthesis of **23**, $CH(OMe)_3$ (η = 0.1 mL/g) was used. Notes: (b) all kinetic plots are for production of **7b**. The inserted reaction time (upper right) does not include workup time (i.e., NRT). In reality, it took approximately 10-20 minutes per one work-up process.

Fig. 5. The MC-synthesis pathway for **Model IV** (UUZU families). Abbrev.: VM: vibration ball milling, w/o-h: without heating. Work-up and/or purification was conducted by column chromatography (CC), extraction (EX), and/or recrystallization (RC). The inserted reaction time (upper right) does not include workup time (i.e., NRT). In reality, it took approximately 10-20 minutes per one work-up process.

Fig. 6. The MC-synthesis pathway for **Model V** (BIOTN families). Abbrev.: VM: vibration ball milling, w/o-h: without heating. Work-up and/or purification was conducted by column chromatography (CC), extraction (EX), and/or recrystallization (RC). The inserted reaction time (upper right) does not include workup time (i.e., NRT). In reality, it took approximately 10-20 minutes per one work-up process.

Fig. 7. Phase transition behavior for **Model I** (a,b), **II** (c,d), **IV** (e), and **V** (f). The corresponding chemical structure and POM images are inserted. Scale bar: 50 µm. Cell thickness: 4 µm. Abbrev.: IL, isotropic liquid; N, nematic; M, mesophase; N_F, ferroelectric nematic; G, glass; K, crystal. Note: (a,b,c) Insets in the N phase are isogyre by conoscopic observation.

Fig. 8. The polarization behavior of **5a**, **14a,** and **22a**. a,d,g) Capacitance properties. Upper: 2D map of capacitance properties; Bottom: capacitance vs temperature. The purple and orange circles denote data scanned on cooling and heating, respectively. b,e,h) *PE* hysteresis loop and its temperature dependence. c,f,i) SHG-hysteresis loop in the N_F phase. The gray line represents *PE*-hysteresis loop as a reference.

Fig. 9. a) The molecular design strategy of DIO variants with no-alkyl chains, C0F2F1F3 (**10b**) and C0F0F1F3 (**10f**), and their classification of phase sequences. b) DSC curves of **10f** on cooling (rate: 5 K min^{-1}). Insets are the corresponding POM images taken under cross polarizers. 2D (c) and 1D WAXD (d,e) profiles in the SmA_F phase (130 °C) for **10f**. The azimuth angle ϕ_1 = 60°, ϕ_2 = 80° represents the scanning range for the generation of the 1D WAXD profile, which is shown in the panel (d) and (e), respectively. The cartoon in panel (d) represents the side view of the SmA_F phase at 130 °C.

Fig. 10. Polarization behavior for C0F0F1F3 (**10f**). The DR spectra: dielectric loss (a) and dielectric permittivity (b); c) dielectric permittivity vs temperature. d) The schematic illustration of the comb-type IPS cell (bottom) for *P*-*E* hysteresis measurement with the PUND waveform *E*-fieldd (top). In the PUND waveform, retention time was set as follows: for OPS: 0, 1, 3, 5, 10, 30, 50, 100, 300 sec; for IPS: 1, 10, 100, 1000 sec. POM images were taken in the comb-type cell with different thicknesses [17 µm (e–g); 4.8 µm (h–j)] in the SmA_F (120 °C) and X_F (112 °C) phases; e,h) initial state (w/o *E*-fieldd) and f,g,i,j) after removal of *E*-field (800 V_{pp} per 500 µm). The kinetics of polarization relaxation in the SmA_F [120 °C, (k)] and X_F [112 °C, (l)] phases. The green and gray plots denote the corresponding kinetics recorded in the IPS and OPS cell, respectively. Insets represent the *P*-*E* hysteresis loops before and after the PUND treatment (t_r = 0 and 1000 s).

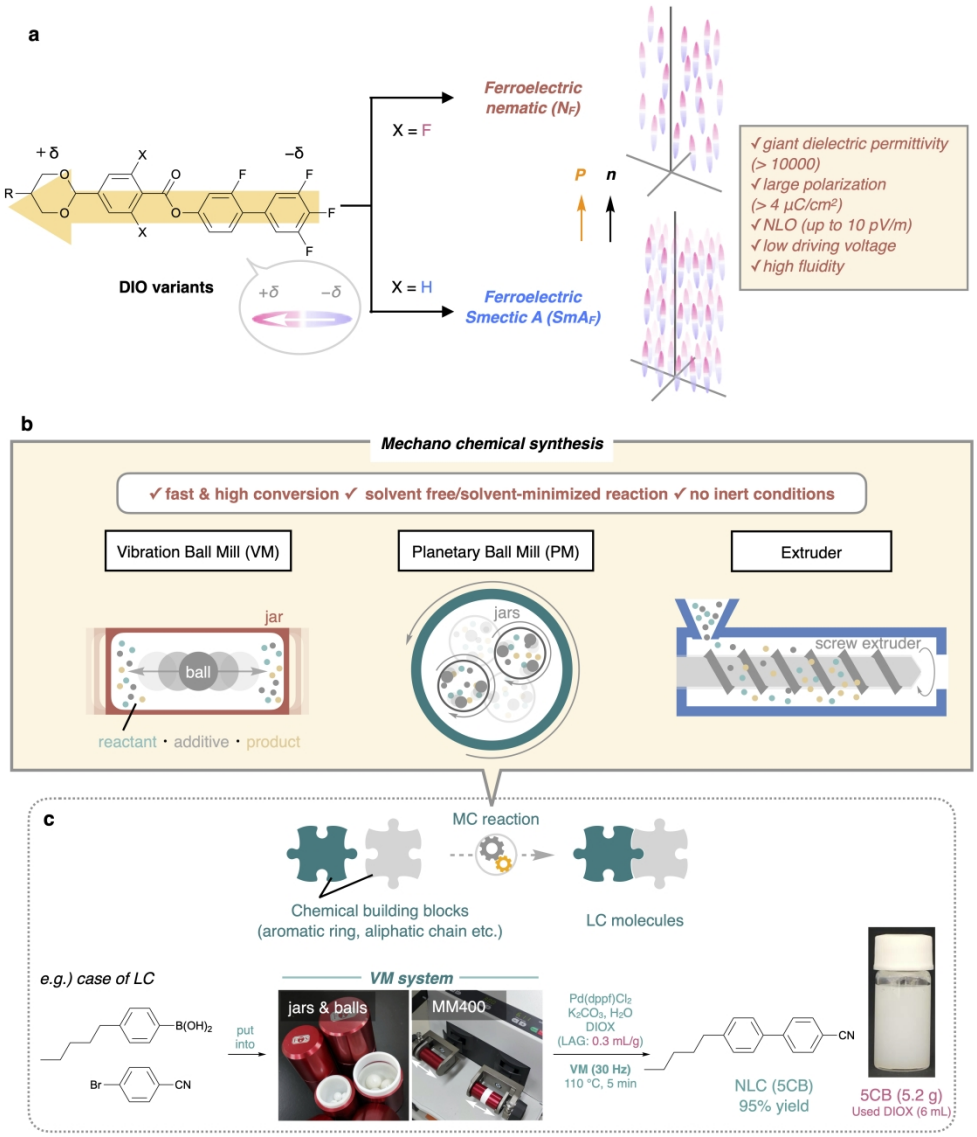

Fig.1

174x198mm (600 x 600 DPI)

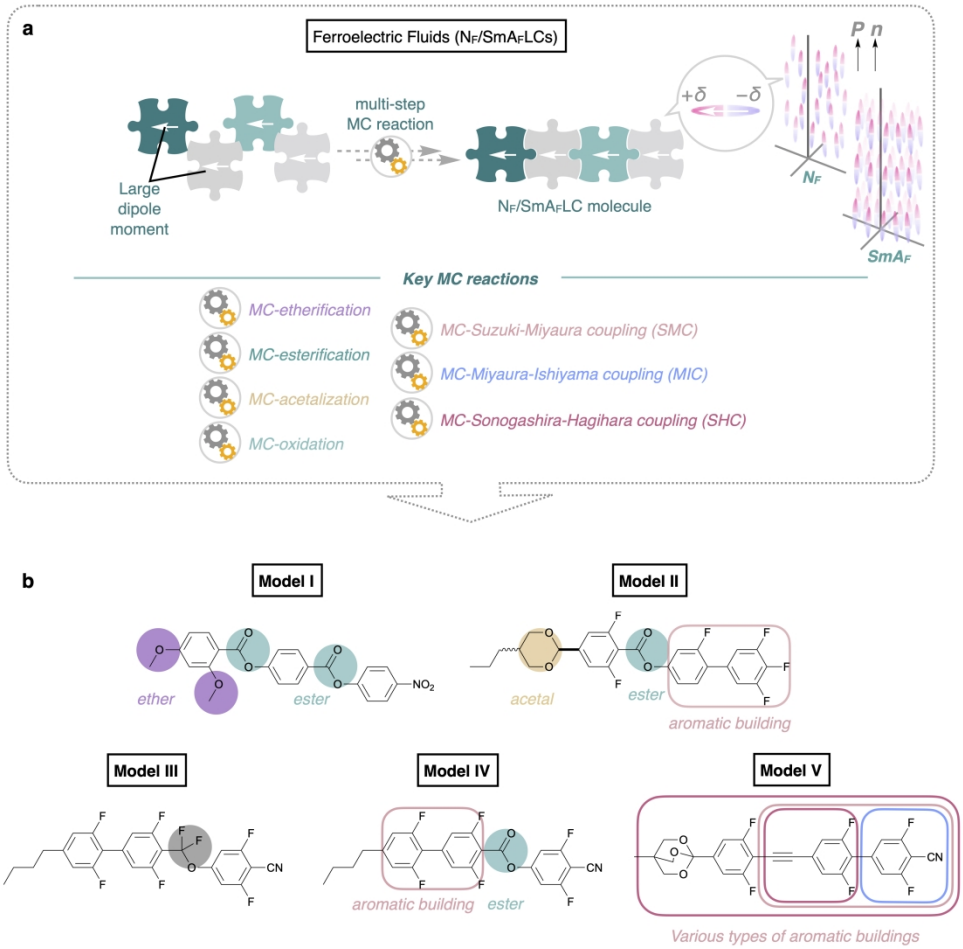

Fig.2

174x166mm (600 x 600 DPI)

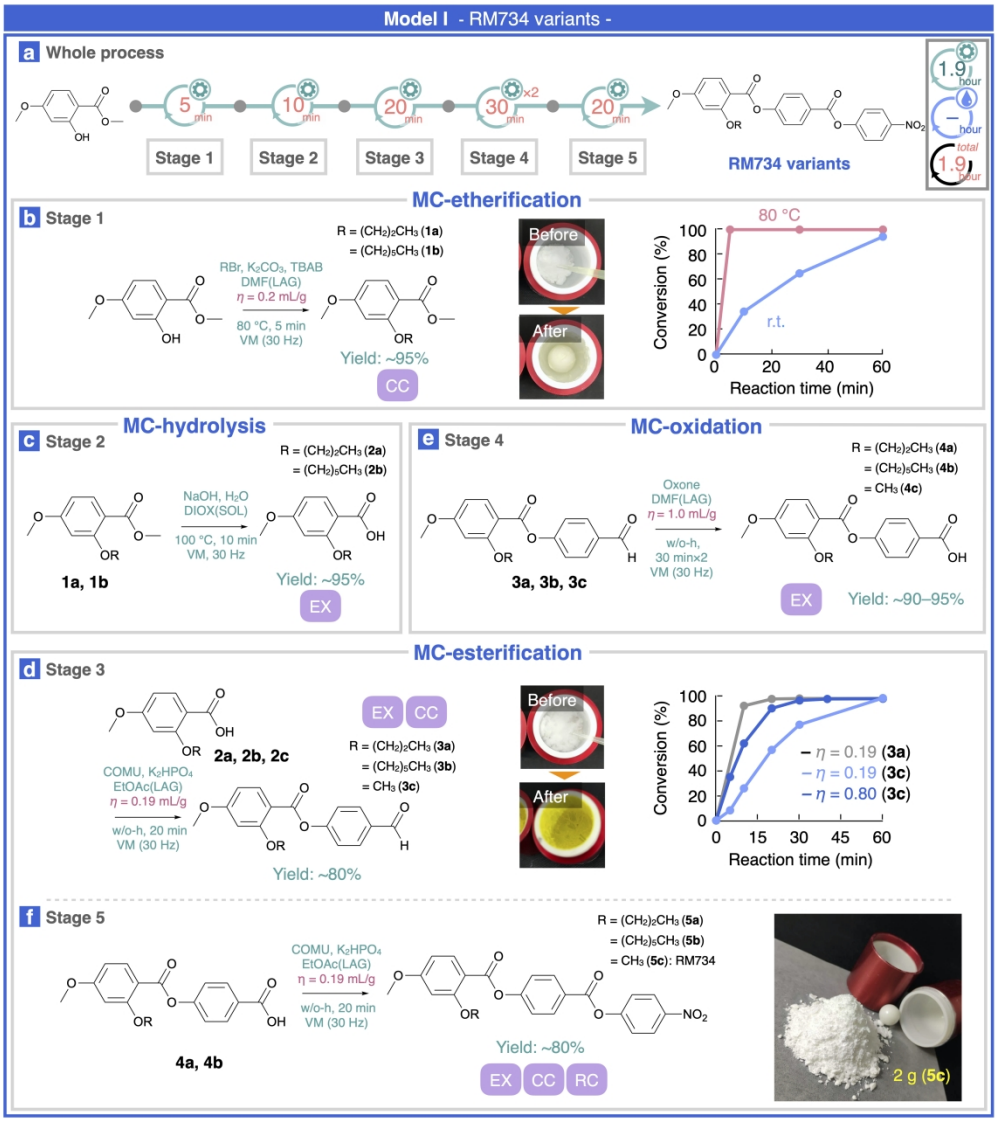

Fig.3

169x189mm (600 x 600 DPI)

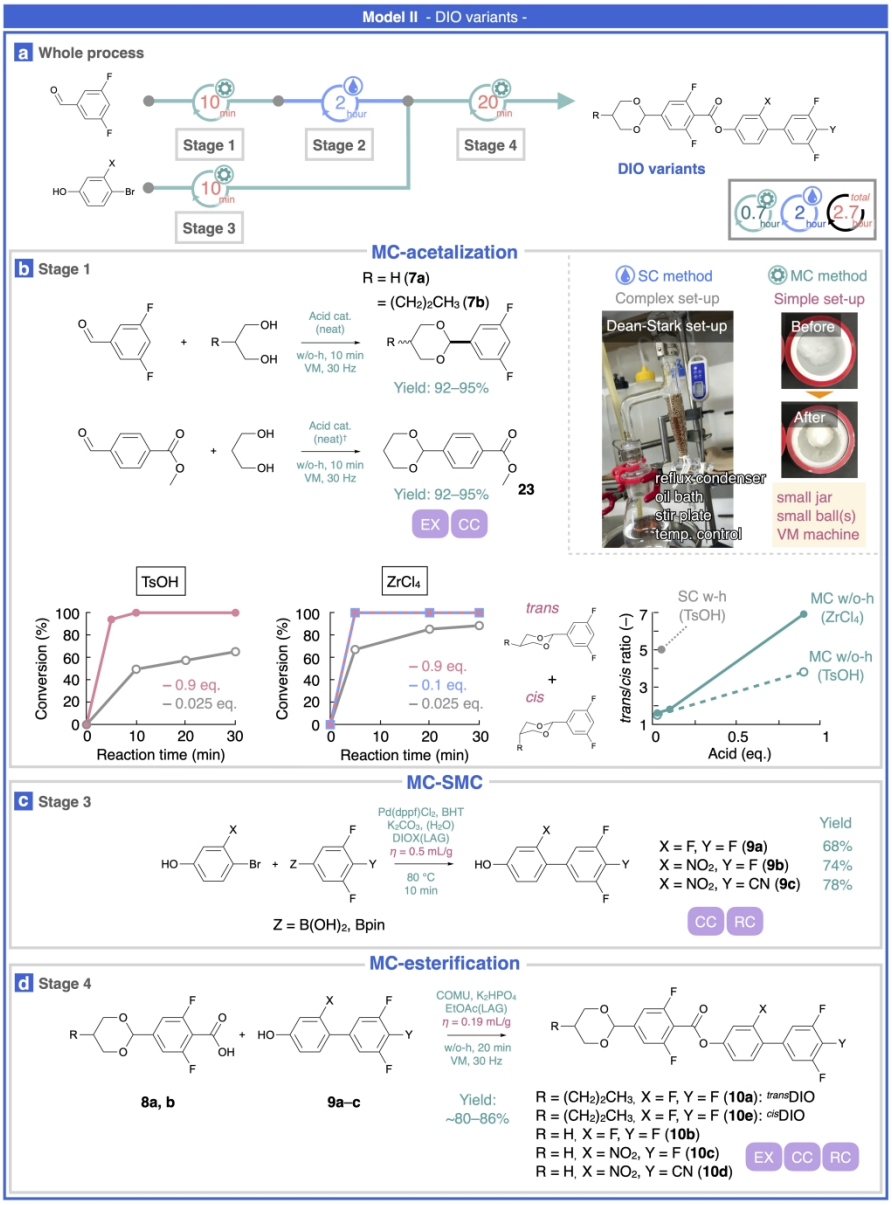

Fig.4

168x227mm (600 x 600 DPI)

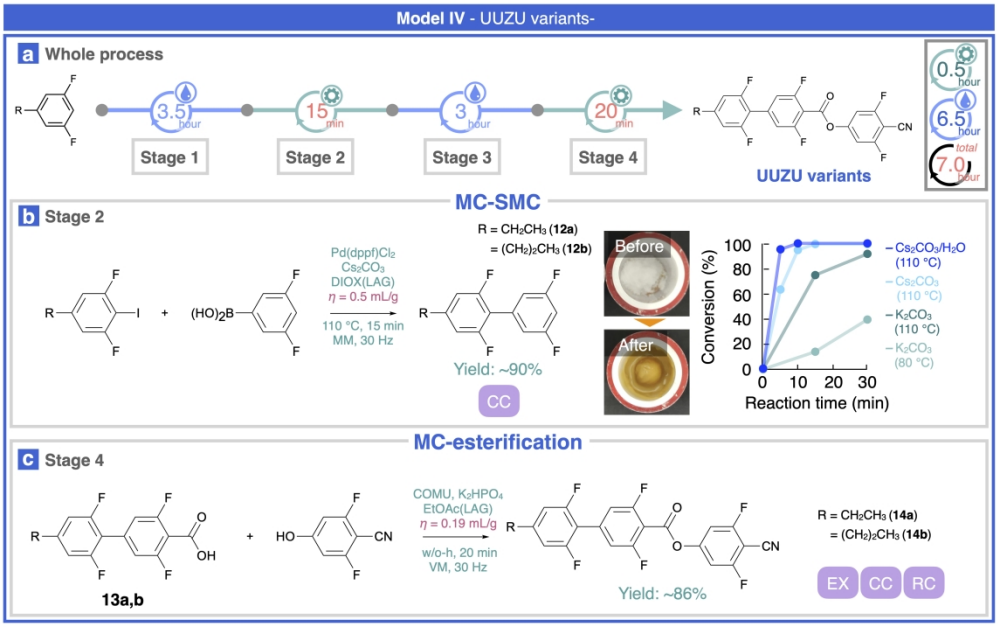

Fig.5

169x106mm (600 x 600 DPI)

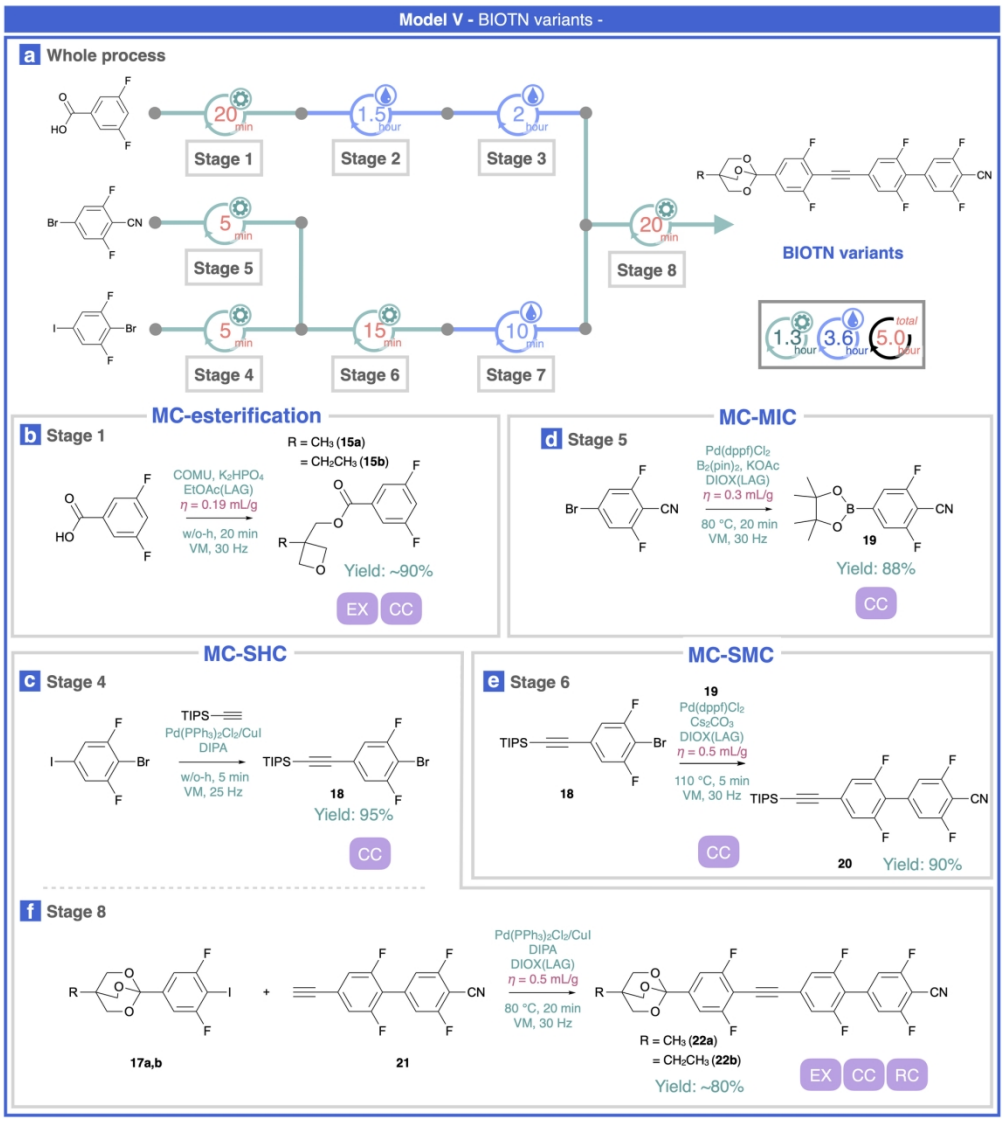

Fig.6

168x187mm (300 x 300 DPI)

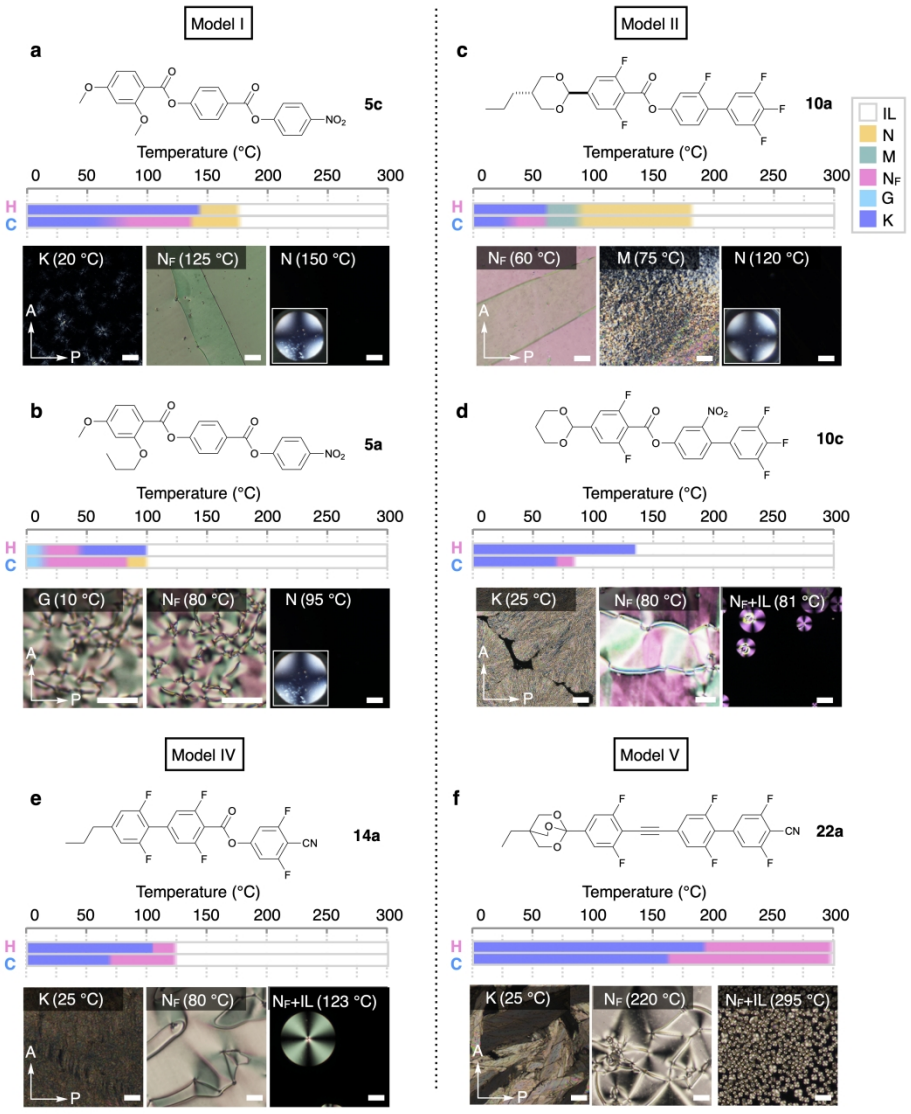

Fig.7

173x194mm (600 x 600 DPI)

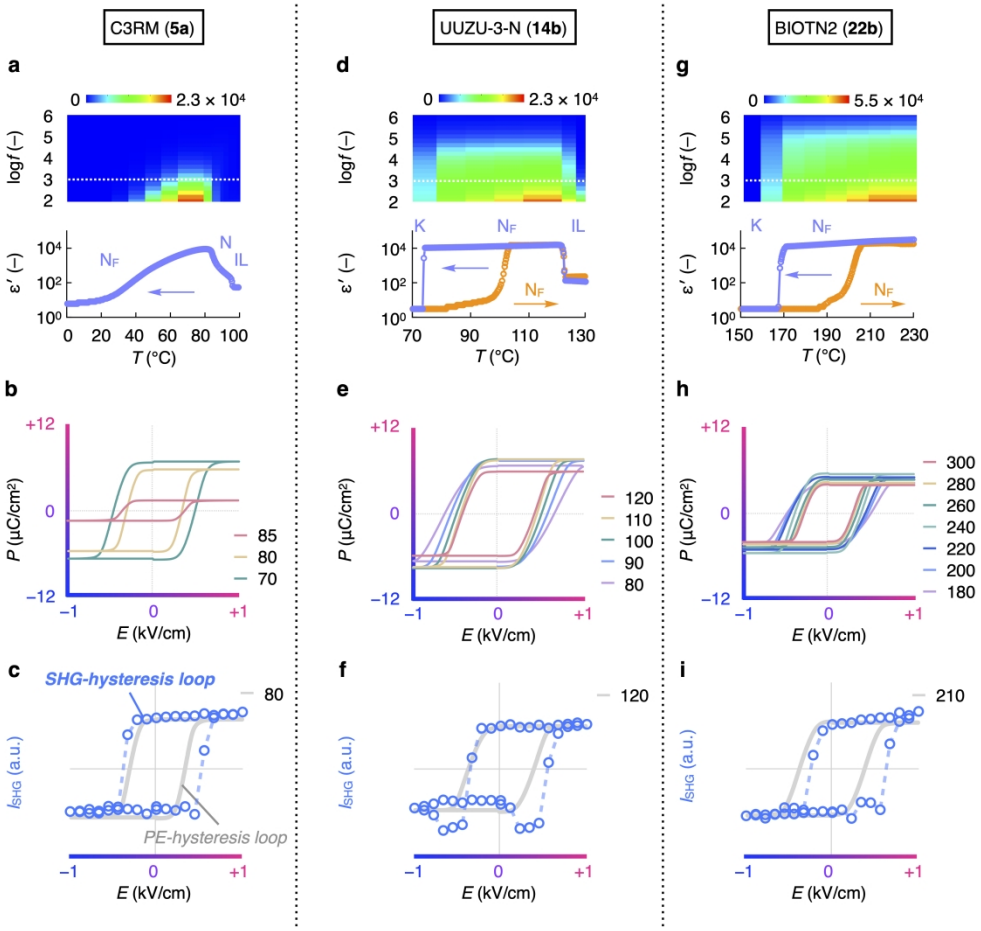

Fig.8

163x155mm (600 x 600 DPI)

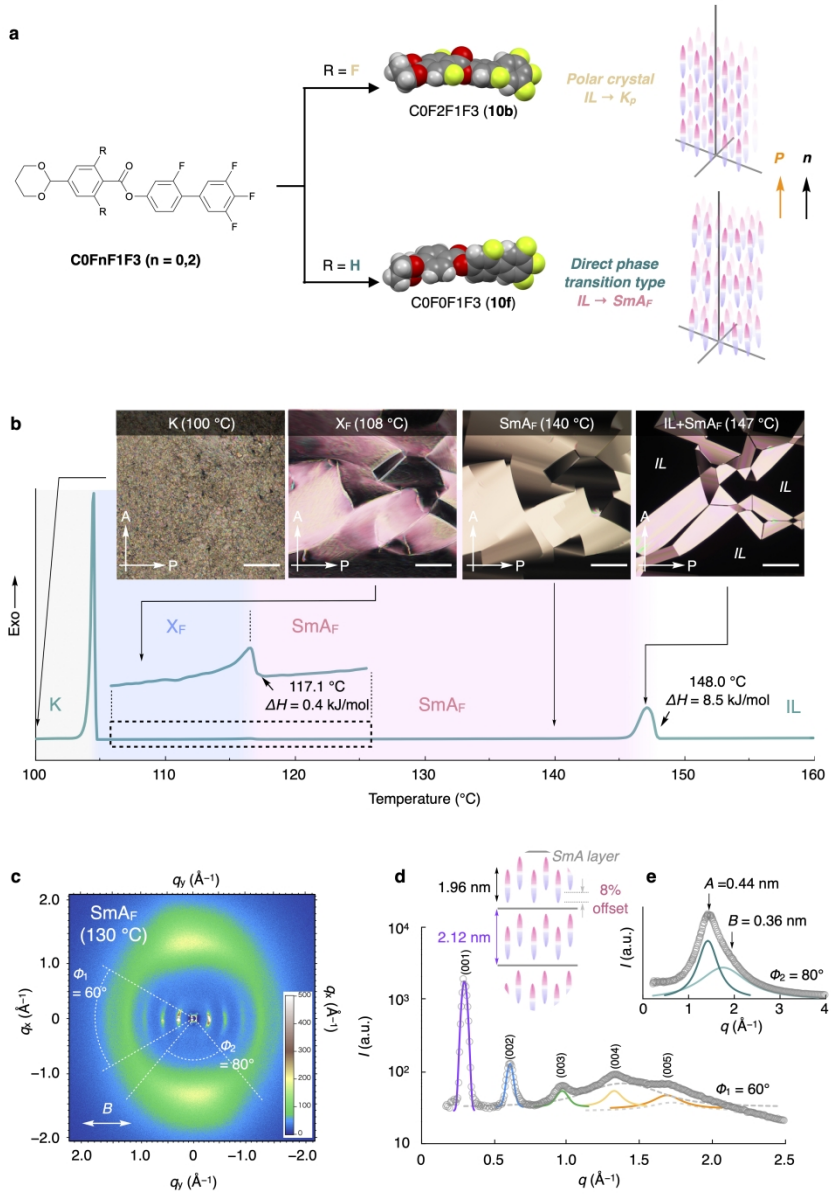

Fig.9

163x231mm (600 x 600 DPI)

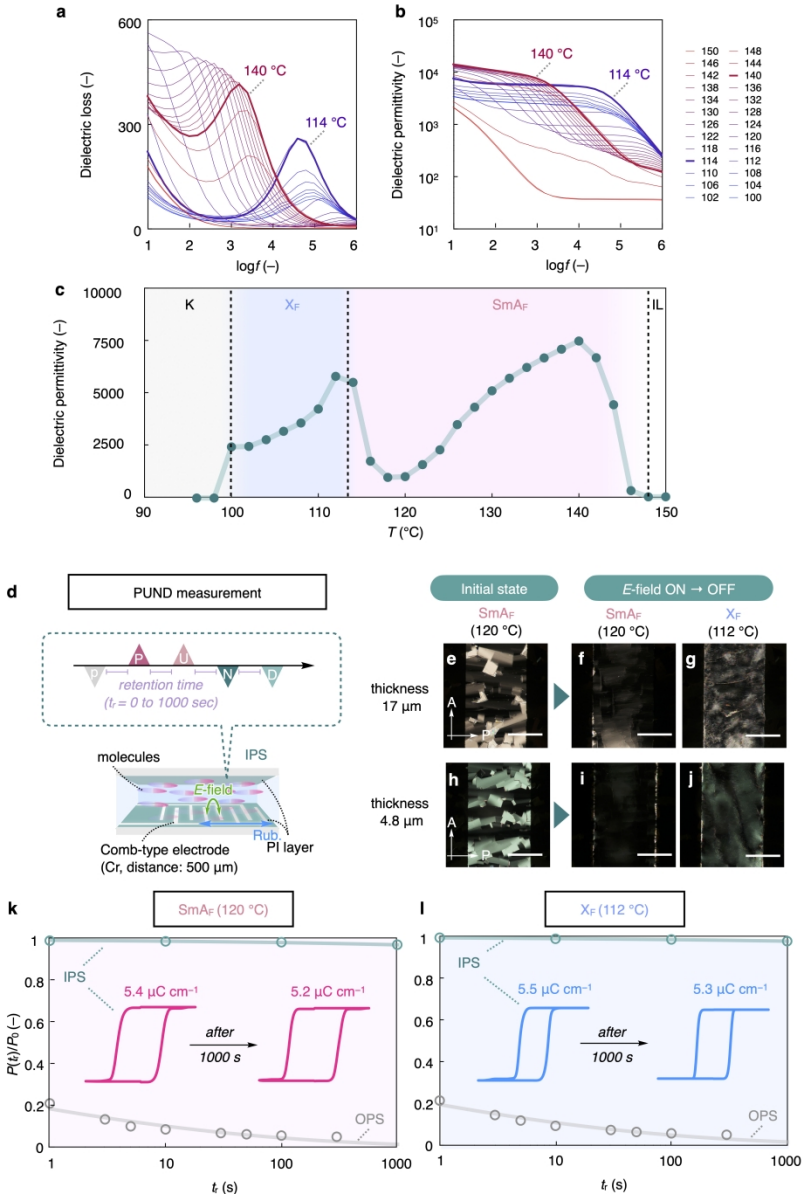

Fig.10

163x243mm (600 x 600 DPI)